Applied Catalysis B: Environmental 247 (2019) 70–77

Contents lists available at ScienceDirect

Applied Catalysis B: Environmental

journal homepage: www.elsevier.com/locate/apcatb

Soluble g-C_3N_4 nanosheets: Facile synthesis and application in photocatalytic hydrogen evolution

Xinhe Wu[a], Xuefei Wang[b], Fazhou Wang[a], Huogen Yu[a,b,*]

[a] State Key Laboratory of Silicate Materials for Architectures, Wuhan University of Technology, Wuhan, 430070, People's Republic of China
[b] School of Chemistry, Chemical Engineering and Life Sciences, Wuhan University of Technology, Wuhan, 430070, People's Republic of China

ARTICLE INFO

Keywords:
g-C_3N_4 nanosheets
H_2-evolution
Photocatalysis
Dispersibility
Solubility

ABSTRACT

The high dispersibility and solubility are highly required for the potential applications and development of well-known g-C_3N_4 material. In this study, a facile hydrothermal treatment and the following vacuum freezing-drying process was developed to synthesize the g-C_3N_4 nanosheets (ca. 5 nm) with excellent dispersibility and solubility in aqueous solutions. It was found that the melem structures with many hydrophilic groups (−NH_2, −OH and −C═O) were formed on the g-C_3N_4 nanosheet surface, resulting in the formation of soluble g-C_3N_4 (SCN) nanosheets. Moreover, the SCN nanosheets can be worked as the effective modifier to greatly increase the H_2-production performance of conventional g-C_3N_4 photocatalyst (the resultant sample was referred to SCN/g-C_3N_4). Photocatalytic results revealed that the SCN/g-C_3N_4 sample exhibited a remarkably higher H_2-production performance than the pure g-C_3N_4 by a factor of ca. 2. The improved H_2-production rate of SCN/g-C_3N_4 photocatalysts could be primarily ascribed to the introduction of hydrophilic groups, which not only remarkably enhances the dispersibility and hydrophilicity of SCN/g-C_3N_4, but also work as the interfacial active sites to accelerate the H^+-reduction reaction and the rapid formation of H_2. The present soluble g-C_3N_4 nanosheets provide potential various applications in environmental protection and energy conversion fields.

1. Introduction

Motivated by the growing awareness of serious environmental pollution and energy crisis, flourishing researches have been conducted on solar energy conversion [1–6]. Semiconductor photocatalysis can utilize solar energy to produce clean energy and repair the environment, which have been praised as one of the most prospective technologies for solving environmental and energy problems [7–12]. As an emerging well-known photocatalyst, graphitic carbon nitride (g-C_3N_4), a metal-free organic polymer semiconductor, has exhibited extensive applications in the fields of degradation of pollutants [13,14], hydrogen production through water splitting [15,16] and CO_2 reduction [17,18] due to its suitable band structure, visible-light adsorption ability and excellent thermochemical stability [19,20]. However, g-C_3N_4 usually exhibits a serious aggregation and low specific surface area owing to the fact that it is usually prepared by a high-temperature polycondensation of suitable precursors [21,22]. Therefore, the g-C_3N_4 nanosheets with a larger specific surface area have been widely synthesized by various methods such as ultrasonic exfoliation [23,24], thermal oxidation exfoliation [25,26] and chemical exfoliation [27]. As a consequence, the resultant g-C_3N_4 nanosheets usually show a larger specific surface area and excellent photocatalytic efficiency. Unfortunately, the above obtained g-C_3N_4 nanosheets usually exhibit a poor dispersibility due to its easy aggregation in the aqueous solution, which seriously restricts their wide applications in photocatalytic fields. Therefore, it is very necessary to explore new strategies to enhance the dispersion of g-C_3N_4 nanosheets for their improved photocatalytic activity.

According to the photocatalytic mechanism, photocatalytic reactions can only occur on the interface between photocatalytic materials and reactants, such as solid-liquid interface or solid-gas interface. Therefore, the effective adsorption of the reactants on the surface of photocatalytic materials has a great impact on the final photocatalytic performance [28–30]. For aqueous systems, developing highly dispersed photocatalytic materials is an effective strategy to improve their interfacial reaction rate owing to its sufficient contact with the reactants in water. As a consequence, many researchers have attempted to develop various methods to enhance the dispersibility of g-C_3N_4 nanosheets. For example, Qiao et al. [31] developed a sonication-exfoliation method in HCl aqueous solution to prepare the proton-

* Corresponding author at: State Key Laboratory of Silicate Materials for Architectures, Wuhan University of Technology, Wuhan, 430070, People's Republic of China.
E-mail address: yuhuogen@whut.edu.cn (H. Yu).

https://doi.org/10.1016/j.apcatb.2019.01.088
Received 10 November 2018; Received in revised form 19 January 2019; Accepted 31 January 2019
Available online 01 February 2019
0926-3373/

functionalized ultrathin g-C_3N_4 nanosheets with excellent dispersion stability. Du et al. [32] proposed an efficient chemical acid (H_2SO_4 and HCl solution) treatment of bulk g-C_3N_4 to obtain soluble acidified graphitic carbon nitride. In addition, Wang et al. [33] demonstrated an efficient pathway of chemical protonation of graphitic carbon nitride in strong oxidizing acids (HNO_3) to obtain a stable g-C_3N_4 colloidal suspension. The above results distinctly reveal that the dispersibility or solubility of resulted g-C_3N_4 nanosheets can be greatly improved after the protonation treatment. However, those reported methods usually include the addition of various acid solutions, which can cause serious environmental issues. Therefore, it is highly required to develop green and facile strategies for the preparation of highly dispersed and soluble g-C_3N_4 nanosheets.

In this article, the soluble g-C_3N_4 (SCN) nanosheets were synthesized by the facile hydrothermal treatment of bulk g-C_3N_4 in a pure water system and the following vacuum freezing-drying process. The prepared SCN nanosheets exhibit high dispersibility and solubility in different solvents due to the introduction of a large amount of hydrophilic groups (-NH_2, −OH and -C = O) and melem structures, which are in situ transformed from the g-C_3N_4 surface during the hydrothermal treatment. Considering their excellent dispersibility and solubility, the above SCN nanosheets can be well coupled on the conventional g-C_3N_4 surface to improve its dispersity via a strong interaction of aromatic Π-delocalization bond. It is interesting to find that after the surface coupling by SCN nanosheets, the resultant SCN/g-C_3N_4 photocatalysts show a great improvement for the H_2-evolution rate. The present work clearly demonstrates a facile and attractive strategy for the preparation of high-dispersibility and solubility g-C_3N_4 nanosheets, which may find various potential developments in the energy and environmental fields.

2. Experimental section

2.1. Preparation of bulk g-C_3N_4 photocatalysts

The bulk g-C_3N_4 photocatalyst was synthesized by a thermal polycondensation of melamine according to our previous reports [34,35]. Briefly, 4 g of melamine (> 99.9%, Alfa Aesar) powder was maintained at 550 °C for 4 h in a muffle furnace. After cooling down to ambient temperature, the resulting yellow bulk was ground into fine powder.

2.2. Preparation of soluble g-C_3N_4 (SCN) nanosheets

The soluble g-C_3N_4 (SCN) nanosheets were prepared by a facile in situ hydrothermal route using the above g-C_3N_4 as the precursor. In detail, 0.4 *g* of the prepared bulk g-C_3N_4 powder was added into 70 mL of deionized water and stirred for 2 h, and then maintained at 180 °C for 12 h. After being naturally cooled down, the remained solid was removed by centrifugation to obtain the supernatant liquid. Finally, the above supernatant liquid was undergone a vacuum freeze-drying process [36,37] to obtain the white fine powder of SCN nanosheets.

2.3. Preparation of SCN/g-C_3N_4 photocatalysts

Considering the excellent solubility and dispersibility of SCN nanosheets due to the existence of a large amount of hydrophilic groups (−NH_2, −OH and −C═O) on its surface, the above SCN nanosheets can be used to modify the dispersibility of conventional g-C_3N_4 photocatalyst. In that case, the above SCN nanosheets are modified on the surface of conventional g-C_3N_4 to form SCN nanosheet-modified g-C_3N_4 (SCN/g-C_3N_4) photocatalyst via a simple ultrasonic method. First, 50 mg of SCN powder was dispersed into 50 mL of lactic acid solution (10 vol%). After heating at 60 °C for 5 min, the SCN powder was dissolved to form a transparent and homogeneous SCN solution (50 mg/50 mL). Second, 50 mg g-C_3N_4 powder was dispersed into 50 mL of deionized water, and then a certain amount of above SCN lactic acid solution was injected quickly. After ultrasonic dispersion for 4 h at ambient temperature, the above suspension was washed and then dried at 60 °C for 10 h to obtain the SCN/g-C_3N_4 photocatalyst.

To further investigate the effect of SCN amounts on the photocatalytic activity of SCN/g-C_3N_4 photocatalyst, the dosage of SCN lactic acid solution (50 mg/50 mL) was controlled to be 0, 50, 150, 250, 400, 500, 2500 and 5000 μL, and the amounts of SCN in the final SCN/g-C_3N_4 were calculated to be 0, 0.1, 0.3, 0.5, 0.8, 1.0, 5.0 and 10 wt%, respectively. In that case, the obtained SCN/g-C_3N_4 sample could be denoted as SCN/g-C_3N_4(Xwt%), where the X referred to the SCN amount.

2.4. Characterization

To observe the morphology, the transmission electron microscope (JEM-2100 F, TEM, JEOL, Japan) and Atomic force microscope (AFM, AR, MFP-3D) were applied. Phase compositions of the as-prepared photocatalyst are confirmed by X-ray powder diffraction (D/MAXRBX, Rigaku Company, Japan). UV–vis spectra are acquired by employing a UV-2450 UV–vis spectrophotometer (SHIMADZU, Japan), where $BaSO_4$ serves as a reflectance criterion. Fourier transform infrared (FTIR) spectra and X-ray photoelectron spectroscopy (XPS) were acquired on a Nexus FT-IR spectrophotometer (Thermo Nicolet, America) and KRATOA XSAM800 XPS system with Mg Kα source, respectively. The thermogravimetric analysis was conducted on a STA-449F3 instrument (Netzsch, Germany).

2.5. Photocatalytic H_2-production activity

The H_2-production rate for various samples is performed in a 100-mL three-necked Pyrex flask, as reported in our previous works [34]. The typical procedures were shown as follows: 50 mg of SCN/g-C_3N_4 (or g-C_3N_4) is dispersed into 80 mL of 10 vol% lactic acid solution (here, lactic acid as a sacrificial regent for hole consumption and Pt (1 wt%) as a cocatalyst), and then is purged with N_2 for 20 min to eliminate the remained O_2. Four 3-W and 420-nm low-power LEDs (Shenzhen Lamplic Science Co. Ltd.) are applied as the visible-light source and continuous stirring is applied to maintain the photocatalysts in suspension state. The produced amount of H_2 is measured by a GC-2014C gas chromatograph (Shimadzu).

3. Results and discussion

3.1. Strategy for the synthesis of soluble g-C_3N_4 (SCN) nanosheets

The soluble g-C_3N_4 (SCN) nanosheets with many hydrophilic groups (-NH_2, −OH and -C = O) can be simply fabricated via the facile hydrothermal treatment of bulk g-C_3N_4 in deionized water and the following vacuum freezing-drying process. The synthetic procedure of SCN nanosheets can be schematically shown in Fig. 1. It is clear that bulk g-C_3N_4 can first be obtained via a thermal polycondensation of melamine precursor [38,39]. Second, the preparedg-C_3N_4 powder was dispersed into deionized water and was hydrothermally treated at 180 °C (Fig. 1A(a–b)). During hydrothermal treatment, the H_2O molecules not only can be incorporated into the interlayers of g-C_3N_4 to cause the depolymerization of bulk g-C_3N_4 and the production of g-C_3N_4 nanosheets, but also can attack its basis tri-s-triazine units to produce melem structures with hydrophilic groups (-NH_2, −OH and -C = O) on the g-C_3N_4 nanosheet surface (Fig. 1B). It is interesting to find that after hydrothermal reaction, most of the bulk g-C_3N_4 is disappeared and only a few products are remained (Fig. 1A(b)). In fact, during hydrothermal treatment (12 h), most of the bulk g-C_3N_4 can be gradually delaminated and deploymerized into the SCN nanosheets that are easily dissolved in water to produce a clear supernatant liquid owing to the existence of various hydrophilic groups (−NH_2, −OH and −C═O) on the sp^2-hybridized carbon (N−C═N) of the aromatic ring

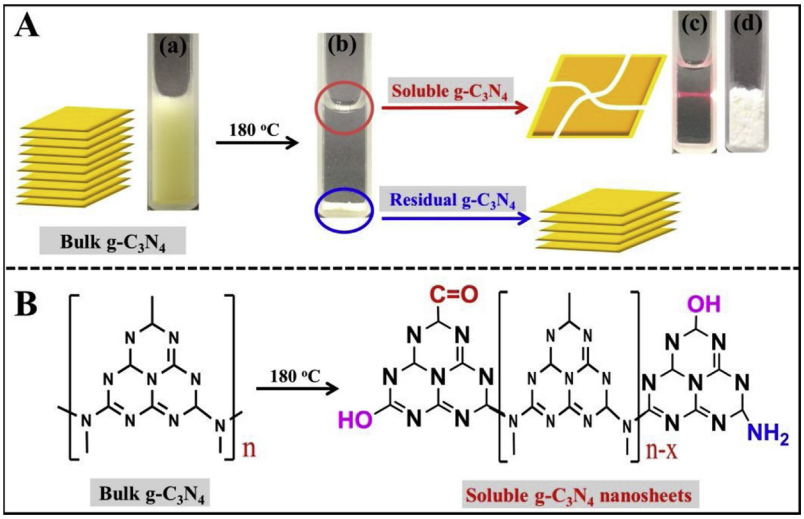

Fig. 1. (A) Graphical illustration for the synthesis of soluble g-C_3N_4 (SCN) nanosheets by a first hydrothermal delamination and its following vacuum freezing-drying technology; (B) the microstructure formation of the soluble g-C_3N_4 (SCN) nanosheets.

[37] (Fig. 1B), while only a few of the residual g-C_3N_4 is remained (with further increasing hydrothermal time to 24 h, the residual g-C_3N_4 can be completely disappeared). To obtain the dissolved SCN nanosheets, the supernatant liquid (Fig. 1A(c)) was obtained by centrifugation to remove the residual g-C_3N_4 solid particles. The presence of SCN nanosheets in the supernatant liquid can be well demonstrated by the obvious Tyndall effect (Fig. 1A(c)). After a vacuum freeze-drying process of the supernatant liquid, the resultant SCN nanosheets were obtained and showed a cotton-like shape (Fig. 1A(d)). Owing to the excellent depolymerization of bulk g-C_3N_4, the resultant SCN nanosheets show a white color, which is completely different to the well-known bulk g-C_3N_4 with a yellow color.

Since the SCN nanosheets are prepared from the above aqueous solution, it is quite interesting to investigate their re-dispersity in various solutions (Fig. S1). In the previous studies [32,33], the g-C_3N_4 nanosheet solutions were only obtained in high-concentration strong oxidizing acids (HNO_3 and H_2SO_4). In this study, it is amazing to find that the prepared SCN nanosheet powder can be easily and directly dissolved in various inorganic acid solutions (such as HCl, H_2SO_4 and HNO_3) with a much lower concentration (ca. 1 mol/L) only via stirring at room temperature for 5 min (Fig. S1(a,b)). Moreover, the resultant SCN nanosheet solutions are very stable even aging for one week, which can be well demonstrated by the well-known Tyndall effect (Fig. S1(c)). In addition to the inorganic acids, the above SCN nanosheets can also be well dissolved into the organic acid solutions. As shown in Fig. S1(d–f), the SCN nanosheets can be completely dissolved in lactic acid or acetic acid solution (10 vol%) by heating at 60 °C for 5 min, and the resulting dispersion solution is still very stable. Therefore, the above results fully suggest that the prepared SCN nanosheets exhibit excellent solubility and stability in various acid solutions owing to the introduction of various hydrophilic groups (−NH_2, −OH and −C═O) on the g-C_3N_4 nanosheet surface.

3.2. Microstructures of soluble g-C_3N_4 (SCN) nanosheets

The formation of above SCN nanosheets can be first demonstrated by the XRD, TEM and AFM results. Compared with the well-known bulk g-C_3N_4 with typical diffraction peaks at 13.1° and 27.4° [14,40], the prepared SCN nanosheets show some new and discernible diffraction peaks that can be matched with melem structures according to the wide reports (Fig. 2A) [41–43]. Further observation suggests that the new diffraction peaks at 17.65°, 26.1°, 28.74° and 29.7° have a slight shift compared with the reported melem structures, which can be ascribed to the introduction of hydrophilic groups (−NH_2, −OH and −C═O) on the surface of melem structures [34]. The corresponding TEM images clearly show that the SCN sample is composed of transparent nanosheets (Fig. 2B and C) with a large size. The curly and wrinkled surface further clearly indicated the ultrathin structure of SCN nanosheets. To clearly reveal the thickness of resultant SCN nanosheets, typical AFM images and its thickness analysis are displayed in Fig. 2D and E. It is obvious that the typical thickness of SCN nanosheets is in the range of 3–5 nm. Obviously, the above results strongly indicated the successful synthesis of ultrathin g-C_3N_4 nanosheets with many hydrophilic groups.

To further demonstrate the existing of melem structure with various hydrophilic groups in the resultant SCN nanosheets, the FTIR and XPS are measured and shown in Fig. 3. The FTIR results (Fig. 3A) indicates that compared with bulk g-C_3N_4, the SCN nanosheets shows many discernible and additional absorption peaks about melem-structure units and hydrophilic groups (-NH_2, −OH and -C = O). Specifically, the strong bands at ca. 1542, 1439 and 769 cm^{-1} are the typical absorptions of melem structures, which can be attributed to the bending and stretching vibrations of C–N heterocycles [44,45], while the absorption peaks at 3469 and 3419 cm^{-1} are assigned to the stretching vibrations of N−H in terminal amine groups [46]. In addition, the two distinct absorption peaks at 1779 and 1735 cm^{-1} can be corresponded to the asymmetric and symmetrical stretching vibrations of C═O group, respectively [47], and the absorption peaks at 1196 and 3343 cm^{-1} can be well matched with the −OH group [48]. On the other hand, the strong absorption peak at 1089 cm^{-1} indicates that the SCN nanosheets have been protonated, which is beneficial for the excellent dispersibility of g-C_3N_4 in the present aqueous solution [49]. Fig. 3B indicates that the XPS O 1s peak in the SCN sample is markedly stronger than that of bulk g-C_3N_4, which can be seen more distinctly in the high-resolution O 1s spectra (Fig. 3C). According to the XPS results (Table 1), the amount of oxygen element in the SCN sample is 10.2 at%, obviously higher than that of bulk g-C_3N_4 (2.3 at.%), which is ascribed to the introduction of −OH and −C═O groups. In fact, compared with the bulk g-C_3N_4, the absorption edge of SCN nanosheets exhibits an obvious blue shift (Fig. 3D), which can be attributed to the excellent delamination and deploymerization of bulk g-C_3N_4 to form the ultrathin SCN nanosheets [32,50]. Therefore, it is very clear that melem groups with many hydrophilic groups (−NH_2, −OH and −C═O) have been *in situ* produced on the g-C_3N_4 nanosheet surface, resulting in the excellent dispersitity and solubility of SCN nanosheets.

The stability of the SCN nanosheets was analyzed by the

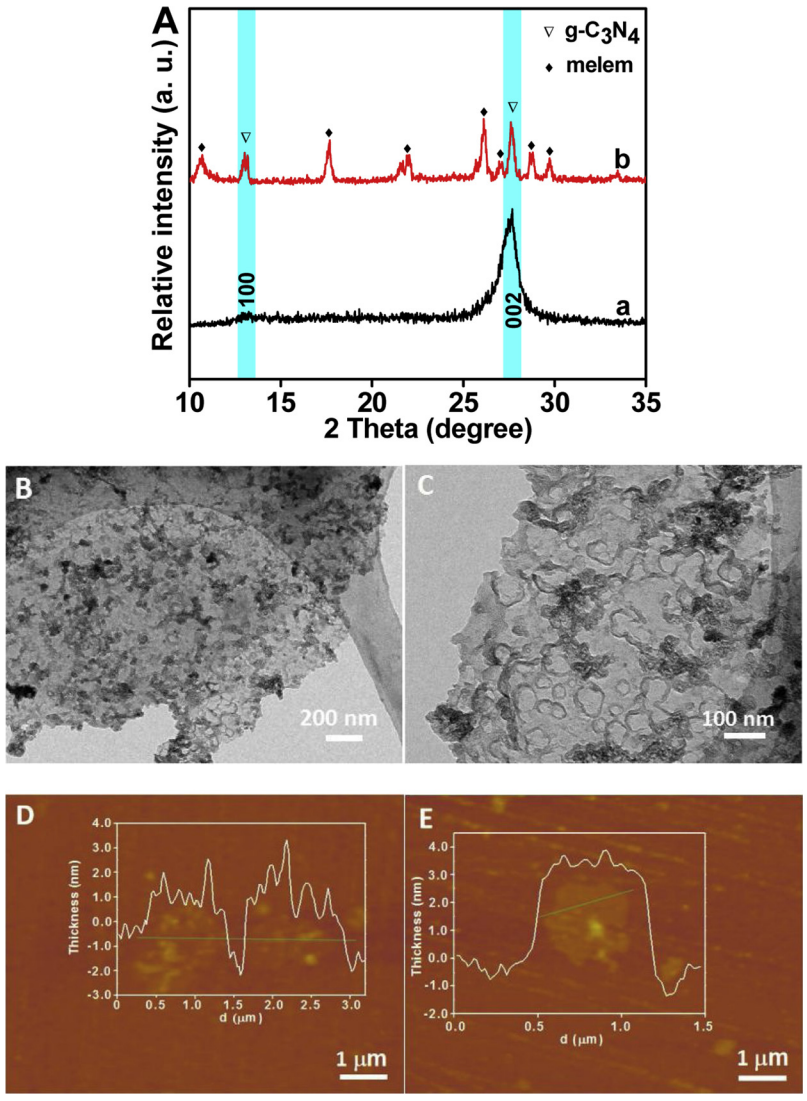

Fig. 2. (A) XRD patterns of (a) g-C_3N_4 and (b) soluble g-C_3N_4 (SCN) nanosheets; Typical (B,C) TEM and (D,E) AFM images of soluble g-C_3N_4 (SCN) nanosheets.

Thermogravimetric analyzer (TG-DSC). For comparison, the bulk g-C_3N_4 is also provided and shown in Fig. 4. For the bulk g-C_3N_4, in the range of 550–750 °C, an obvious mass loss of ca. 98.77 wt% and a maximum endothermic peak at 724 °C can be found, which can be assigned to the complete decomposition of bulk g-C_3N_4, in good agreement with the previous results [34]. For the SCN nanosheets, its DSC curve shows more endothermic peaks than that of bulk g-C_3N_4, which is completely different to the bulk g-C_3N_4. A wide endothermic peak below 200 °C can be attributed to the desorption of H_2O or −OH in the SCN nanosheets. Besides, an endothermic peak at 319.7 °C and the corresponding mass loss of ca. 51.61 wt% are clearly observed, which can be due to the decomposition and removal of melem structures on the SCN nanosheets. However, compared with the widely reported decomposition temperature (450 °C) of melem structures [41,42], the present endothermic peak (319.7 °C) has an obvious decrease owing to the introduction of oxygen-containing groups (−C═O and −OH) on the melem surface. According to its TG curve, the amount of melem structures in the SCN nanosheets can be estimated to be ca. 51.61 wt%, clearly suggesting that a lot of melem structures with hydrophilic groups (−NH_2, −OH and −C═O) are formed on the g-C_3N_4 nanosheets during hydrothermal treatment. In addition, another obvious endothermic peak at 385.2 °C and the coincident mass loss of ca. 38.94 wt % can be found, which can be ascribed to the decomposition of the residual C–N heterocyclic structure of the SCN nanosheets. In fact, it should be noted that the present endothermic peak (385.2 °C) is much lower than that of bulk g-C_3N_4 (724 °C) owing to the excellent depolymerization of bulk g-C_3N_4 and the production of SCN nanosheets.

3.3. Application of soluble g-C_3N_4 (SCN) nanosheets in photocatalytic H_2 evolution of bulk g-C_3N_4

Based on the above results, the resultant soluble g-C_3N_4 (SCN) nanosheets exhibit an excellent dispersibility and solubility in the aqueous solution owing to the introduction of many hydrophilic groups (−NH_2, −OH and −C═O). Therefore, it is very meaningful to investigate the potential application of the SCN nanosheets in photocatalytic field. Considering the poor hydrophilicity of conventional bulk g-C_3N_4 photocatalyst obtained from a high-temperature calcination method, here, the present SCN nanosheets were used to modify the dispersibility of conventional g-C_3N_4 photocatalyst with the aiming of improving the photocatalytic H_2-production performance. In this study, the clear SCN solution was directly added into the conventional g-C_3N_4 suspension by ultrasonic dispersion for 4 h. For comparison, the bulk g-C_3N_4 photocatalyst without the addition of SCN nanosheets are also prepared under an identical condition. It is clear that the g-C_3N_4 without SCN nanosheets (Fig. 5A) has almost completely precipitated, while the g-C_3N_4 with the addition of SCN nanosheets (Fig. 5B) exhibits a stable suspension in deionized water even after aging for 4 h. It is believed

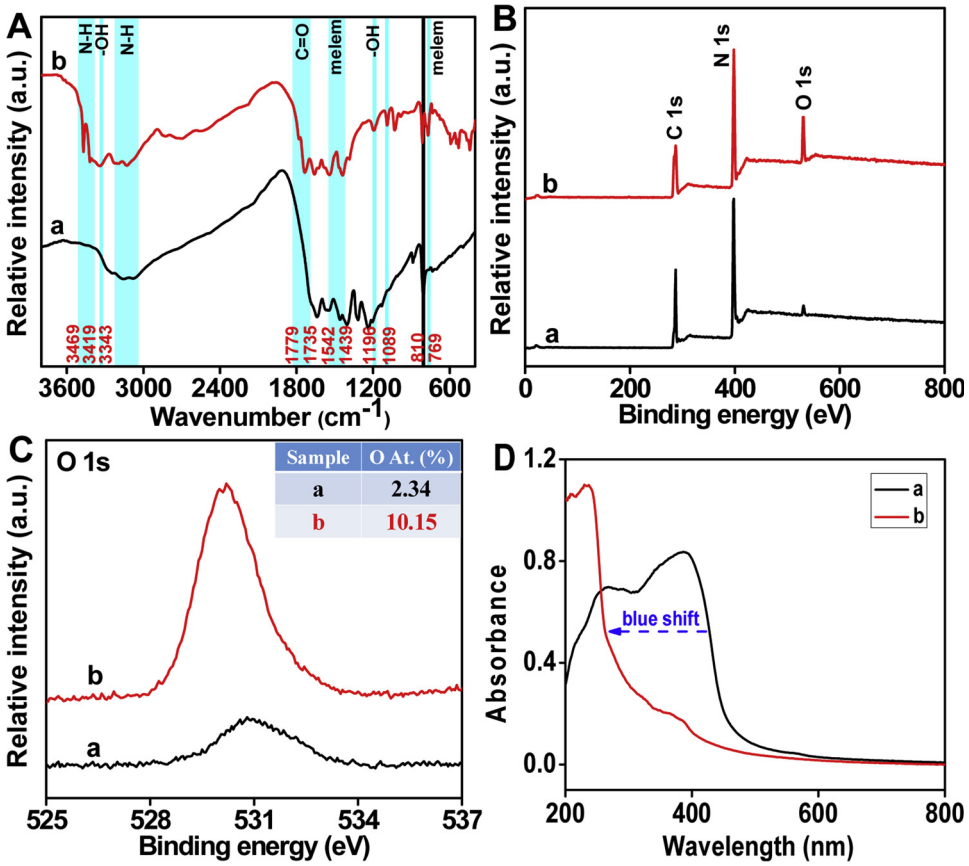

Fig. 3. (A) FTIR spectra, (B) XPSsurvey spectra, (C) O 1s high-resolution XPS spectra and (D) UV–vis diffused reflectance spectra of (a) bulk g-C_3N_4 and (b) soluble g-C_3N_4 (SCN) nanosheets.

Table 1
The element components of various samples according to XPS results.

Sample	C	N	O
SCN	44.57	45.29	10.15
g-C_3N_4	43.93	53.72	2.34
SCN/g-C_3N_4(0.1 wt%)	44.15	53.25	2.60
SCN/g-C_3N_4(0.3 wt%)	43.58	53.39	2.95
SCN/g-C_3N_4(1 wt%)	44.25	52.79	3.03
SCN/g-C_3N_4(5 wt%)	42.80	53.14	4.07

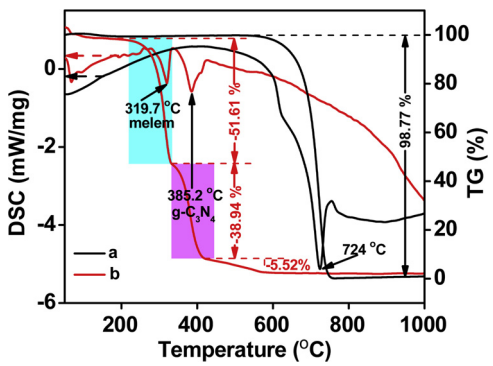

Fig. 4. TG and DSC curves for the (a) bulk g-C_3N_4 and (b) soluble g-C_3N_4 (SCN) nanosheets.

that the SCN nanosheets can be strongly coupled on the g-C_3N_4 surface via a strong interaction of aromatic Π-delocalization bond [51,52], causing the excellent dispersibility of the resultant SCN/g-C_3N_4 composite. The strong coupling between the SCN nanosheets and g-C_3N_4 surface can be well demonstrated by its TEM images, as shown in Fig. 5C and D. It can be seen clearly that compared with the smooth surface of bulk g-C_3N_4 (Fig. S2), many cotton-shaped SCN nanosheets have been successfully loaded on the g-C_3N_4 surface, leading to the formation of SCN/g-C_3N_4 photocatalyst. Therefore, the SCN/g-C_3N_4 photocatalyst with excellent dispersibility can be easily synthesized by directly adding the SCN nanosheets into the conventional g-C_3N_4 suspension.

The XRD and XPS were conducted to further certify the formation of SCN/g-C_3N_4 composite. Fig. 6 shows the XRD patterns of conventional g-C_3N_4 and SCN/g-C_3N_4 samples. It is clear that there are no extra diffraction peaks in the SCN/g-C_3N_4 samples except for the typical diffraction peaks (27.4° and 13.1°) of g-C_3N_4 [53,54], which may be related to the low contents of SCN nanosheets. Fig. 7A shows the typical XPS survey spectra of g-C_3N_4 and SCN/g-C_3N_4 samples. It is clear that in addition to the C and N element from the g-C_3N_4, all samples exhibit the characteristic peaks of O 1 s. For the g-C_3N_4 sample, the oxygen element primarily comes from the adsorbed H_2O, while that of the SCN/g-C_3N_4 is mainly from the SCN nanosheets with oxygen-containing hydrophilic groups (-C = O and −OH). To further explore the variation of oxygen contents, Fig. 7B exhibits the O 1 s high-resolution XPS spectra of various samples. Compared with bulk g-C_3N_4, the XPS peaks of O elements gradually increase with the addition of more hydrophilic nanosheets. According to Table 1, the amounts of oxygen element in the g-C_3N_4, SCN/g-C_3N_4(0.1 wt%), SCN/g-C_3N_4(0.3 wt%), SCN/g-C_3N_4(1 wt%) and SCN/g-C_3N_4(5 wt%) photocatalysts are 2.34, 2.60, 2.95, 3.03 and 4.07 at%, respectively.

To further analyze the composition of the SCN/g-C_3N_4 composite, a typical TG-DSC of SCN/g-C_3N_4 sample is conducted, as shown in Fig. 8. Compared with the bulk g-C_3N_4 with a typical endothermic peak at 728.0 °C (Fig. 4a), a new endothermic peak at 334.6 °C is observed for

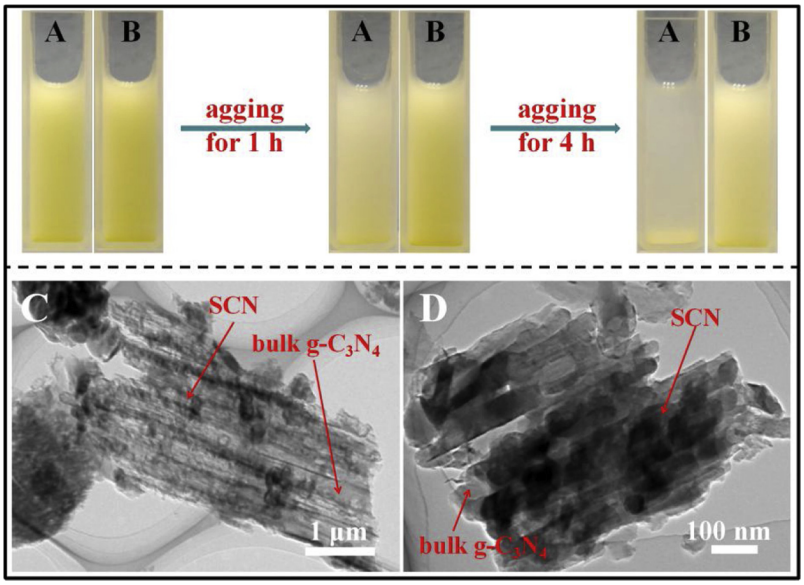

Fig. 5. (A) Graphical illustration for the coupling of bulk g-C_3N_4 with soluble g-C_3N_4 (SCN) nanosheets; (B) The optical pictures of (a) g-C_3N_4 and (b) SCN/g-C_3N_4; (C, D) TEM images of the SCN/g-C_3N_4(0.3 wt%).

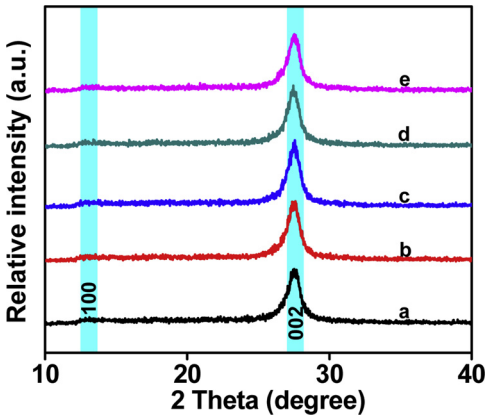

Fig. 6. XRD patterns of various samples: (a) g-C_3N_4, (b) SCN/g-C_3N_4(0.1 wt%), (c) SCN/g-C_3N_4(0.3 wt%), (d) SCN/g-C_3N_4(1 wt%) and (e) SCN/g-C_3N_4(5 wt%).

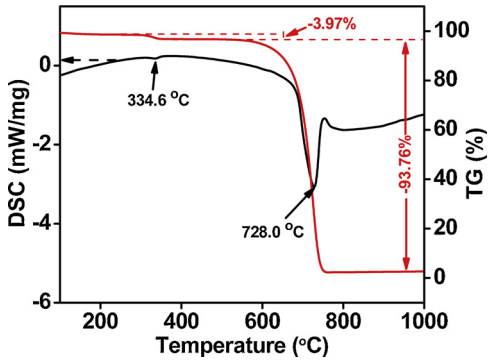

Fig. 8. TG and DSC curves for the SCN/g-C_3N_4(5 wt%) sample.

the SCN/g-C_3N_4(5 wt%) sample, which can be attributed to the decomposition of SCN nanosheets, in good agreement with the results of SCN nanosheets (319.7 °C in Fig. 4b). According to the TG curve in the range of 300–450 °C, the amount of SCN nanosheets can be calculated to be 3.97 wt%.

The light-absorption performance of g-C_3N_4 and SCN/g-C_3N_4 samples was characterized by UV–vis DRS (Fig. 9). It is found that the absorption edge of g-C_3N_4 and its band gap (2.70 eV) are similar to the previous reports [55]. After coupling with the SCN nanosheets, the absorption spectra of the resultant SCN/g-C_3N_4 samples and their corresponding photographs show no obvious distinction compared with the pure g-C_3N_4. As a consequence, the following different photocatalytic activity of SCN/g-C_3N_4 samples can only be ascribed to the presence of SCN nanosheets.

On the basis of the above results, it is very necessary and meaningful to explore the H_2-production performances of SCN/g-C_3N_4 photocatalysts. The H_2-evolution performance of SCN/g-C_3N_4 photocatalysts

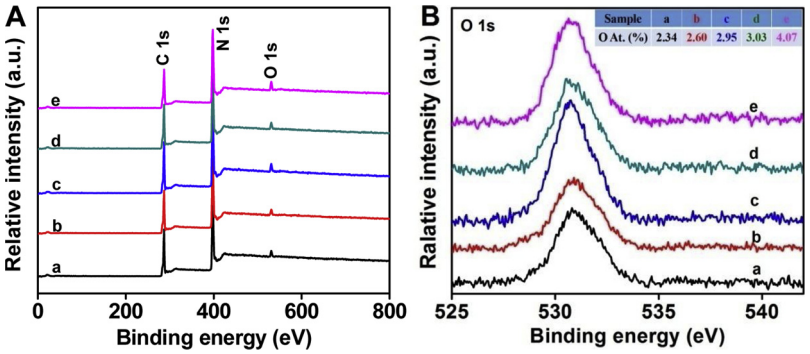

Fig. 7. (A) XPS survey spectra and (B, C) O 1 s high-resolution XPS spectra of various samples: (a) g-C_3N_4, (b) SCN/g-C_3N_4(0.1 wt%), (c) SCN/g-C_3N_4(0.3 wt%), (d) SCN/g-C_3N_4(1 wt%) and (e) SCN/g-C_3N_4(5 wt%).

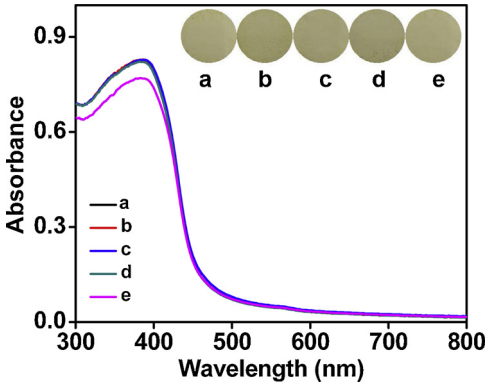

Fig. 9. UV–vis diffused reflectance spectra and their corresponding photographs of various samples: (a) g-C_3N_4, (b) SCN/g-C_3N_4(0.1 wt%), (c) SCN/g-C_3N_4(0.3 wt%), (d) SCN/g-C_3N_4(1 wt%) and (e) SCN/g-C_3N_4(5 wt%).

was evaluated under visible-light irradiation using Pt (1 wt%) as a co-catalyst. Fig. 10A exhibits the photocatalytic H_2-evelution rate of SCN nanosheets, bulk g-C_3N_4 and SCN/g-C_3N_4samples. It is found that the SCN nanosheets show no photocatalytic H_2-production performance owing to the absence of visible-light absorption (white color), which is consistent with its UV–vis spectrum (Fig. 3D), and the bulk g-C_3N_4 exhibits a low H_2-evolution rate of 8.9 μmol h^{-1}. After coupling with SCN nanosheets, the H_2-production rate of SCN/g-C_3N_4 photocatalyst shows a significant increase, and the SCN/g-C_3N_4(0.3 wt%) shows the highest performance with a H_2-production rate of 17.98 μmol h^{-1}, which is about 2 times higher than that of g-C_3N_4. Further increase of the SCN contents causes the decreased photocatalytic H_2-production performance of the SCN/g-C_3N_4. In addition, the recycling experiments of the bulk g-C_3N_4 and SCN/g-C_3N_4(0.3 wt%) samples were conducted and the results were shown in Fig. 10B, which reveals the fact that the SCN/g-C_3N_4 sample can maintain excellent photocatalytic stability for H_2 production. To further comfirm the stability of SCN/g-C_3N_4 during the photocatalytic test, after photocatalytic H_2-evolution reaction, the SCN/g-C_3N_4(5 wt%) was first separated from the reaction solution, washing, drying, and then was used to measure its TG-DSC (Fig. S3). It is found that compared with the as-prepared SCN/g-C_3N_4 sample (Fig. 8), similar TG and DSC curves can also be found in the SCN/g-C_3N_4 after photocatalytic reaction (Fig. S3). Especially, an obvious endothermic peak at 356.3 °C with a corresponding mass loss of ca. 3.7 wt% can be attributed to the decomposition of SCN nanosheets, clearly suggesting the well coupling and stability of SCN nanosheets on the g-C_3N_4 surface.

The above results distinctly reveal that the H_2-production performance of bulk g-C_3N_4 can be significantly increased by the introduction of SCN nanosheets with many hydrophilic groups. Apparently, according to the TEM images, XPS, UV–vis, and TG-DSC results, it is believed that the increased hydrophilic groups (−NH_2, −OH and −C═O) in the SCN/g-C_3N_4 photocatalysts should be the most vital factor for the greatly enhanced photocatalytic activity. On one hand, the hydrophilic groups on the SCN/g-C_3N_4 surface can obviously enhance the dispersibility of SCN/g-C_3N_4 photocatalyst via the formation of hydrogen bond with water molecules. On the other hand, the oxygen-containing hydrophilic groups (−C═O and −OH) can enrich H^+ from aqueous solution, and then work as the interfacial active sites to promote the H^+-reduction reaction and the rapid formation of H_2 [56]. Therefore, the SCN/g-C_3N_4 photocatalyst obviously exhibits an enhanced photocatalytic activity compared with the bulk g-C_3N_4.

To further investigate the improved H_2-production mechanism of SCN/g-C_3N_4 photocatalyst, the transient photocurrent responses (i–t curve) and electrochemical impedance spectroscopy (EIS) of various samples were measured, as revealed in Fig. S4. It can be clearly found that compared with the SCN nanosheets and conventional g-C_3N_4 photocatalyst, the SCN/g-C_3N_4(0.3 wt%) photocatalyst shows an enhanced photocurrent density and a smaller arc radius for the EIS plots, indicating a faster interfacial oxidation reaction of photogenerated holes and a rapider transportation rate of photogenerated carriers in the SCN/g-C_3N_4(0.3 wt%) photocatalyst. Obviously, it can be deduced that the higher transfer efficiency and rapider interfacial catalytic reactions of photoinduced charges contribute to the increased H_2-production rate of the resultant SCN/g-C_3N_4 photocatalyst.

4. Conclusions

A facile hydrothermal technology and its following vacuum freezing-drying process has been proposed to successfully synthesize the soluble g-C_3N_4 (SCN) nanosheets. It was found that the melem structures with many hydrophilic groups (−NH_2, −OH and −C═O) were formed on the g-C_3N_4 nanosheets, resulting in the high dispersibility and solubility of the SCN nanosheets in various solvents. The resultant SCN nanosheets can be used as the effective modifier to improve the dispersibility of conventional g-C_3N_4. Photocatalytic results suggested that the resultant SCN/g-C_3N_4 photocatalysts clearly showed a remarkably improved H_2-production activity, and the SCN/g-C_3N_4(0.3 wt%) exhibited the highest H_2-evolution activity, which is significantly higher than the pure g-C_3N_4 by a factor of 2. The improved H_2-production rate of SCN/g-C_3N_4 photocatalyst can be mainly ascribed to introduction of melem structure with many oxygen-containing hydrophilic groups, which can effectively improve the dispersibility of SCN/g-C_3N_4 photocatalyst and adsorb H^+ from aqueous solution and then work as the interfacial active sites to improve the H_2-production reaction.

Acknowledgements

This work was supported by the National Natural Science Foundation of China (21771142, 51472192, and 21477094). This work was also financially supported by the Fundamental Research Funds for the Central Universities (WUT 2017IB002).

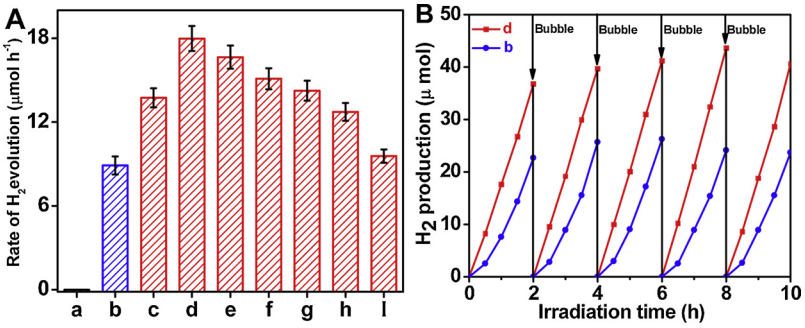

Fig. 10. (A) The photocatalytic H_2-production activities of various samples: (a) SCN, (b) bulk g-C_3N_4, (c) SCN/g-C_3N_4(0.1 wt%), (d) SCN/g-C_3N_4(0.3 wt%), (e) SCN/g-C_3N_4(0.5 wt%), (f) SCN/g-C_3N_4(0.8 wt%), (g) SCN/g-C_3N_4(1 wt%), (h) SCN/g-C_3N_4(5 wt%) and (I) SCN/g-C_3N_4(10 wt%); (B) Photocatalytic cycling test of typical (b) g-C_3N_4 and (d) SCN/g-C_3N_4(0.3 wt%) photocatalysts.

Appendix A. Supplementary data

Supplementary material related to this article can be found, in the online version, at doi:https://doi.org/10.1016/j.apcatb.2019.01.088.

References

[1] M. Kuehnel, K. Orchard, K. Dalle, E. Reisner, J. Am. Chem. Soc. 139 (2017) 7217–7223.
[2] Y. Kuwahara, N. Furuichi, H. Seki, H. Yamashita, J. Mater. Chem. A 5 (2017) 18518–18526.
[3] T. Wu, P. Wang, J. Qian, Y. Ao, C. Wang, J. Hou, Dalton Trans. 46 (2017) 13793–13801.
[4] Y. Li, Y. Bian, H. Qin, Y. Zhang, Z. Bian, Appl. Catal. B: Environ. 206 (2017) 293–299.
[5] Y. Wang, X. Zhao, D. Cao, Y. Wang, Y. Zhu, Appl. Catal. B: Environ. 211 (2017) 79–88.
[6] M. Wen, K. Mori, Y. Kuwahara, T. An, H. Yamashita, Appl. Catal. B: Environ. 218 (2017) 555–569.
[7] F. Cheng, H. Yin, Q. Xiang, Appl. Surf. Sci. 391 (2017) 432–439.
[8] Q. Wang, J. He, Y. Shi, S. Zhang, T. Niu, H. She, Y. Bi, Z. Lei, Appl. Catal. B: Environ. 214 (2017) 158–167.
[9] H. Yu, W. Liu, X. Wang, F. Wang, Appl. Catal. B: Environ. 225 (2018) 415–423.
[10] P. Wang, T. Wu, C. Wang, J. Hou, J. Qian, Y. Ao, ACS Sus. Chem. Eng. 5 (2017) 7670–7677.
[11] C. Tang, L. Liu, Y. Li, Z. Bian, Appl. Catal. B: Environ. 201 (2017) 41–47.
[12] P. Wang, Y. Sheng, F. Wang, H. Yu, Appl. Catal. B: Environ. 220 (2018) 561–569.
[13] Z. Wei, F. Liang, Y. Liu, W. Luo, J. Wang, W. Yao, Y. Zhu, Appl. Catal. B: Environ. 201 (2017) 600–606.
[14] R. Hao, G. Wang, H. Tang, L. Sun, C. Xu, D. Han, Appl. Catal. B: Environ. 187 (2016) 47–58.
[15] Y. Li, X. Feng, Z. Lu, H. Yin, F. Liu, Q. Xiang, J. Colloid Interface Sci. 513 (2018) 866–876.
[16] H. Yu, P. Xiao, P. Wang, J. Yu, Appl. Catal. B: Environ. 193 (2016) 217–225.
[17] J. Wen, J. Xie, X. Chen, X. Li, Appl. Surf. Sci. 391 (2017) 72–123.
[18] B. Zhu, P. Xia, Y. Li, W. Ho, J. Yu, Appl. Surf. Sci. 391 (2017) 175–183.
[19] J. Xu, Z. Wang, Y. Zhu, ACS Appl. Mater. Interfaces 9 (2017) 27727–27735.
[20] J. Wen, J. Xie, H. Zhang, A. Zhang, Y. Liu, X. Chen, X. Li, ACS Appl. Mater. Interfaces 9 (2017) 14031–14042.
[21] W. Liu, J. Shen, X. Yang, Q. Liu, H. Tang, Appl. Surf. Sci. 456 (2018) 369–378.
[22] X. Bai, C. Sun, S. Wu, Y. Zhu, J. Mater. Chem. A 3 (2015) 2741–2747.
[23] K. Schwinghammer, M.B. Mesch, V. Duppel, C. Ziegler, J. Senker, B.V. Lotsch, J. Am. Chem. Soc. 136 (2014) 1730–1733.
[24] J. Coleman, Acc. Chem. Res. 46 (2013) 14–22.
[25] P. Niu, L. Zhang, G. Liu, H. Cheng, Adv. Funct. Mater. 22 (2012) 4763–4770.
[26] F. Dong, Y. Li, Z. Wang, W. Ho, Appl. Surf. Sci. 358 (2015) 393–403.
[27] J. Seo, Y. Jun, S. Park, H. Nah, T. Moon, B. Park, J. Kim, Y. Kim, J. Cheon, Angew. Chem., Int. Ed. 46 (2007) 8828–8831.
[28] H. Yu, W. Zhong, X. Huang, P. Wang, J. Yu, ACS Sus. Chem. Eng. 6 (2018) 5513–5523.
[29] S. Liu, C. Liu, W. Wang, B. Cheng, J. Yu, Nanoscale 4 (2012) 3193–3200.
[30] H. Yu, W. Chen, X. Wang, Y. Xu, J. Yu, Appl. Catal. B: Environ. 187 (2016) 163–170.
[31] T.Y. Ma, Y. Tang, S. Dai, S.Z. Qiao, Small 10 (2014) 2382–2389.
[32] X. Du, G. Zou, Z. Wang, X. Wang, Nanoscale 7 (2015) 8701–8706.
[33] J. Zhang, M. Zhang, L. Lin, X. Wang, Angew. Chem., Int. Ed. 127 (2015) 6395–6399.
[34] X. Wu, F. Chen, X. Wang, H. Yu, Appl. Surf. Sci. 427 (2018) 645–653.
[35] X. Wang, J. Cheng, H. Yu, J. Yu, Dalton Trans. 46 (2017) 6417–6424.
[36] Y. Wang, W. Jiang, W. Luo, X. Chen, Y. Zhu, Appl. Catal. B: Environ. 237 (2018) 633–640.
[37] W. Jiang, Q. Ruan, J. Xie, X. Chen, Y. Zhu, J. Tang, Appl. Catal. B: Environ. 236 (2018) 428–435.
[38] Q. Xu, C. Jiang, B. Cheng, J. Yu, Dalton Trans. 46 (2017) 10611–10619.
[39] L. Zhang, G. Wang, Z. Xiong, H. Tang, C. Jiang, Appl. Surf. Sci. 436 (2018) 162–171.
[40] B. Zhu, J. Zhang, C. Jiang, B. Cheng, J. Yu, Appl. Catal. B: Environ. 207 (2017) 27–34.
[41] E. Wirnhier, M.B. Mesch, J. Senker, W. Schnick, Chem. Eur. J. 19 (2012) 2041–2049.
[42] B. Jürgens, E. Irran, J. Senker, P. Kroll, H. Müller, W. Schnick, J. Am. Chem. Soc. 125 (2003) 10288–10300.
[43] B.V. Lotsch, M. Döblinger, J. Sehnert, L. Seyfarth, J. Senker, O. Oeckler, W. Schnick, Chem. Eur. J. 13 (2007) 4969–4980.
[44] S. Chu, C. Wang, J. Feng, Y. Wang, Z. Zou, Int. J. Hydrogen Energy 39 (2014) 13519–13526.
[45] H. Sun, G. Zhou, Y. Wang, A. Suvorova, S. Wang, ACS Appl. Mater. Interfaces 6 (2014) 16745–16754.
[46] W. Gu, F. Lu, C. Wang, S. Kuga, L. Wu, Y. Huang, M. Wu, ACS Appl. Mater. Interfaces 9 (2017) 28674–28684.
[47] P. Wang, J. Wang, X. Wang, H. Yu, J. Yu, M. Lei, Y. Wang, Appl. Catal. B: Environ. 132-133 (2013) 452–459.
[48] R. Gang, Y. Ding, J. Xu, C. Tao, L. Zhong, Nanotechnol. 22 (2011) 055705.
[49] Y. Zhang, A. Thomas, M. Antonietti, X. Wang, J. Am. Chem. Soc. 131 (2009) 50–51.
[50] L. Corp, W. Schlenker, J. Am. Chem. Soc. 23 (139) (2017) 7904–7912.
[51] Y. Chen, J. Zhang, M. Zhang, X. Wang, Chem. Sci. 4 (2013) 3244–3248.
[52] M. Zhang, X. Wang, Energy Environ. Sci. 7 (2014) 1902–1906.
[53] F. Chen, H. Yang, W. Luo, P. Wang, H. Yu, Chinese J. Catal. 38 (2017) 1990–1998.
[54] L. Lu, G. Wang, M. Zou, J. Wang, J. Li, Appl. Surf. Sci. 441 (2018) 1012–1023.
[55] F. Chen, H. Yang, X. Wang, H. Yu, Chinese J. Catal. 38 (2017) 296–304.
[56] L. Ming, H. Yue, L. Xu, F. Chen, J. Mater. Chem. A 2 (2014) 19145–19149.